NANO: Brief Reports and Reviews
Vol. 14, No. 4 (2019) 1950041 (11 pages)

DOI: 10.1142/S1793292019500413

World Scientific
www.worldscientific.com

Amorphous Bimetallic Nanowires with High-Performance Microwave Absorption: A Case for FeCo Nanowires

Junyao Shen*, Yongtao Yao*, Yanju Liu† and Jinsong Leng*,‡
*National Key Laboratory of Science and Technology
on Advanced Composites in Special Environments
Harbin Institute of Technology
No. 2 YiKuang Street, Harbin 150080, P. R. China

†Department of Astronautical Science and Mechanics
Harbin Institute of Technology
No. 92 West Dazhi Street, Harbin 150001, P. R. China
‡lengjs@hit.edu.cn

Received 2 November 2018
Accepted 25 February 2019
Published 3 April 2019

Amorphous FeCo nanowires (NWs) with the average diameter of 120 nm were successfully prepared with a magnetic-field-assisted (MFA) hydrothermal method. Rapid reaction time was adopted to obtain amorphous FeCo NWs, being checked by XRD and TEM. Tuning the stoichiometric ratio of Fe/Co content meets the optimal impedance matching under different absorption frequency, making both improved intensities and frequency ranges of microwave absorption. For example, under 3 mm coating thickness, the reflection loss (RL) peaks of Fe_3Co_7, Fe_5Co_5 and Fe_7Co_3 NWs are −25.88 dB at 4 GHz, −19.06 dB at 4.24 GHz and −21.98 dB at 5.44 GHz. The related efficient absorption bandwidths ($f_E < -10$ dB) of Fe_3Co_7 NWs, Fe_5Co_5 NWs and Fe_7Co_3 NWs are 5.40 GHz, 3.52 GHz and 4.91 GHz, respectively. It is ascribed to integrating enhanced dielectric/conductive losses, negligible damages from eddy current effect and good impedance matching for high-performance FeCo NWs absorbers. This work paves a new path on synthesizing bimetallic wire-like nanostructures for microwave absorption demands.

Keywords: FeCo nanowires; amorphous structures; magnetic properties; microwave absorbing.

1. Introduction

To date, daily portable devices, such as laptops, remote controllers and smart cellphones, are vulnerable to being disturbed from GHz-level electromagnetic interference (EMI).[1–4] Not to mention that related electromagnetic (EM) pollutions severely harm the human being's health.[5,6] Nowadays, nanostructured bimetallic absorbers, like FeCo,[7–9] FeNi,[10–12] and CoNi,[13,14] are of great interest in recent choices for advanced microwave absorbers. These bimetallic absorbers can break through the low saturation magnetizations of monometallic ones,[14,15] which boost magnetic loss for the electromagnetic wave (EMW) absorption ability. A suitable choice is

‡Corresponding author.

exploring novel FeCo absorber, which owns the highest saturation magnetization in the 3d transition binary alloy reports (245 emu g^{-1}).[16,17] Meantime, diverse FeCo micro/nanostructures, such as wire-like,[18] flower-like[19] and dendritic-like structures,[20] have been reported for synergizing with magnetic, dielectric, and conductive losses. In general, one-dimensional (1D) nanostructures are meritorious to improve subsequent microwave absorption performance, being originated from the high surface-to-volume ratio. It can supply abundantly interfacial polarizations,[21] microcurrent loss,[22] and abundant active sites for multireflection and scattering.[23,24] It often involves templated-assisted synthesis routes like using surfactants[25] and anodic aluminum oxide (AAO)[16,26,27] for preparing 1D FeCo-based nanostructures, leaving some disadvantages to affect related EMW absorption. The purity of FeCo nanowires is vulnerable to the disturbance of the organic/inorganic residuals from hard/soft templates.[16,28] It harms the subsequent EMW absorption performance with hard-removal nonmagnetic residuals. Besides, tedious preparation and removal processes of template-assisted routes usually need strong acid/base agents and second calcination.[26,27,29] It is still a big challenge for green synthesis of 1D FeCo nanostructures to meet microwave absorption on demands.

For microwave absorption, external microwave undergoes two stages for absorption: (a) being captured by the absorber and (b) being transformed other energies in the absorber (e.g., heat). Thus, it requires ideal absorbers to possess excellent trapping abilities of space charge and to endow enough converting time of attenuating the entered EMW via various forms of polarization.[1,3,5] It prompts the motivation of constructing amorphous nanostructures with abundant defects to induce additional surface/interface polarizations via doping and encapulsating.[30,31] Due to embedding secondary mediums, crystal lattices of the absorber are distorted to affect the unit cell volume.[32] It eventually induces the fluctuation of dielectric constants for tuning dielectric loss.[32,33] It has been proved the welfares of amorphous carbon-based composites for improving EMW absorption ability.[34,35] However, the reports on amorphous bimetallic absorbers are rare, especially for wire-like nanostructures. A full-scale consideration is still needed to investigate microwave absorption behaviors of 1D bimetallic absorbers, being related to the benefits of both amorphous and wire-like structures.

Herein, we report surfactant-free amorphous FeCo nanowires (NWs) with an magnetic-field-assisted (MFA) hydrothermal route for tunable microwave absorption demands. Amorphous FeCo NWs reserve uniform distributions of substructured FeCo particles with the average size of ~120 nm. The average length is up to 3–5 μm, presenting high aspect ratio. Amorphous structure of FeCo NWs supplies enough dielectric loss and to repel eddy current effect for good magnetic loss. Progressed microwave absorption intensity and bandwidth are also achieved through tuning the atomic ratios of Fe/Co.

2. Experimental

2.1. *Chemicals*

The adopted agents, containing iron chloride tetrahydrate ($FeCl_2 \cdot 4H_2O$), cobalt chloride hexahydrate ($CoCl_2 \cdot 6H_2O$) and sodium borohydride ($NaBH_4$), were acquired from Aladdin Industrial Inc., China. The deionized water was self-made by the laboratory with the resistivity of 15 MΩ cm. Any further purification was unemployed in the chosen chemicals with analytical grade.

2.2. *Synthesis of amorphous FeCo NWs*

The agent, sodium borohydride, acted as the reducer for synthesis amorphous hierarchical FeCo NWs via MFA hydrothermal method. The mole ratios of iron and cobalt elements were precisely controlled as 3:7, 1:1 and 7:3, respectively. FeCo NWs were labeled as Fe_3Co_7 NWs, Fe_5Co_5 NWs and Fe_7Co_3 NWs, being consistent with the stoichiometric ratio of Fe:Co. Typically, synthesis process of Fe_5Co_5 NWs was implemented as follows. The mixture of 0.99 g $FeCl_2 \cdot 4H_2O$ and 1.19 g $CoCl_2 \cdot 6H_2O$ was added into a three-neck flask for configuring a 10-mL solution. After vigorously stirring, the concentration doses of 15 mM $NaBH_4$ were added slowly. Then it was set with a 10-min agitation for the solution. The intensity of the magnetic field was 0.4 T. After the solution being transferred into the Teflon-lined vessel, a piece of black floccule was produced under 2 min with the hydrothermal temperature of 80°C. Then as-prepared floccule was washed through deionized water and ethanol for each three times and be collected after filtration. Black products were finally dried at 90°C under vacuum condition overnight.

2.3. *Characterization of amorphous FeCo NWs*

Microstructures of three FeCo NWs were analyzed with CuKα radiation of powder X-ray diffraction (XRD) system ($\lambda = 0.15405$ nm). Surface morphologies were determined on FEI Quanta 200F Field-emission scanning electron microscopy (FESEM). The transmission electron microscopy (TEM) and high-resolution transmission electron microscopy (HRTEM) images were obtained with G2 F20-type microscopy operating at 200 kV with equipping energy disperse spectrometer (EDS) accessory (FEI Co., USA).

Elements' analyses of amorphous FeCo NWs were depended to the EDS accessory. Magnetic properties of FeCo NWs were tested from a vibrating sample magnetometer (Quantum Design, USA) under room temperature. The measured magnetic field range was from -20 kOe to $+20$ kOe.

To measure electromagnetic properties, FeCo NWs were homogeneously dispersed in the paraffin matrix, making FeCo NWs occupy 80 wt.% in total mass. FeCo NWs/paraffin composites were suppressed as toroidal-bodied specimens with the inner/outer diameters of 3.04 mm and 7.00 mm. The S parameters, marked as S11, S12, S21 and S22, were checked on a type-N5234A vector network analyzer from 2 GHz to 18 GHz. It is according to the transmission/reflection coaxial line method. Under different thicknesses, reflection loss (RL) values are based on the subsequent equations[36]:

$$Z_{\text{in}} = (\mu_r/\varepsilon_r)^{1/2} \tanh[j(2\pi fd/c)](\mu_r\varepsilon_r)^{1/2}], \quad (1)$$

$$\text{RL} = 20 \log |(Z_{\text{in}} - 1)/(Z_{\text{in}} + 1)|, \quad (2)$$

where f is the frequency of EM wave, d is the coating thickness of the absorbers and c is in charge of the speed of light in free space condition. Z_{in} represents the input impedance of the absorbent. ε_r and μ_r are the complex permittivity and permeability of the materials, respectively.

3. Results and Discussion

3.1. *Morphology and characterization of FeCo NWs*

In this paper, amorphous FeCo nanowires were prepared via the MFA hydrothermal condition. The reduction involved the following chemical equations[37]:

$$\text{NaBH}_4 + 2\text{H}_2\text{O} \rightarrow \text{NaBO}_2 + 4\text{H}_2\uparrow, \quad (3)$$

$$\text{Fe}^{2+} + \text{Co}^{2+} + 4\text{BO}_2^- + 4\text{H}_2\text{O} + 2\text{H}_2 \rightarrow \text{FeCo}\downarrow + 4\text{B(OH)}_3. \quad (4)$$

It usually produces pure FeCo nanoparticles (NPs) with no surfactants and hard templates.[38,39] Herein, we infer the primary FeCo particles were accumulated to form the wire-like nanostructure under the magnetic lines of force driven,[40] being originated from the external magnetic field. For obtaining amorphous structures, the nucleation and growth theory has been proven; the amorphous particles can be fast prepared before crystallization of the final product through suppressing total Gibbs free energy.[41] Thus, we finally obtained the amorphous FeCo NWs under a rapid reaction time condition. It is a facile and eco-friend approach to construct FeCo NWs with no using of surfactants and AAO template for inducing 1D nanostructure. The method is no needed of subsequent treatments like the second calcination and washing of strong acid/base agents.

Figure 1 shows micromorphologies of Fe_3Co_7 NWs, Fe_5Co_5 NWs and Fe_7Co_3 NWs under low-magnification and high-magnification FESEM images. It presents that shapes of all three FeCo NWs retain wire-like hierarchy micro/nanostructures. Average diameter and length of three samples are $\sim$120 nm and 3–5 μm, respectively.

The XRD patterns (Fig. 2) prove that three FeCo NWs are amorphous structures due to the absences of featured Fe and Co peaks in all these

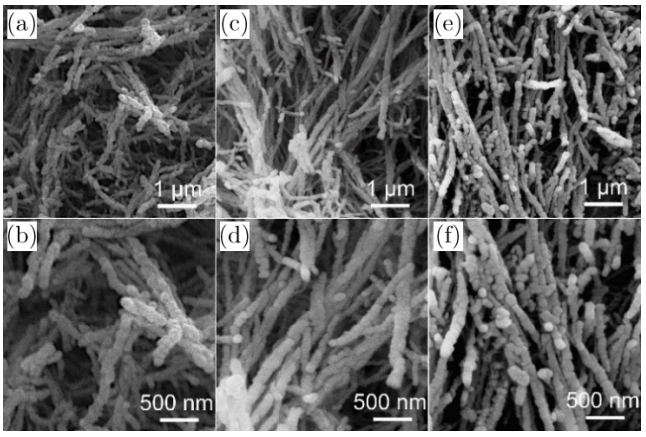

Fig. 1. Low/high-magnification SEM images of FeCo NWs. (a, b) Fe_3Co_7 NWs; (c, d) Fe_5Co_5 NWs; (e, f) Fe_7Co_3 NWs.

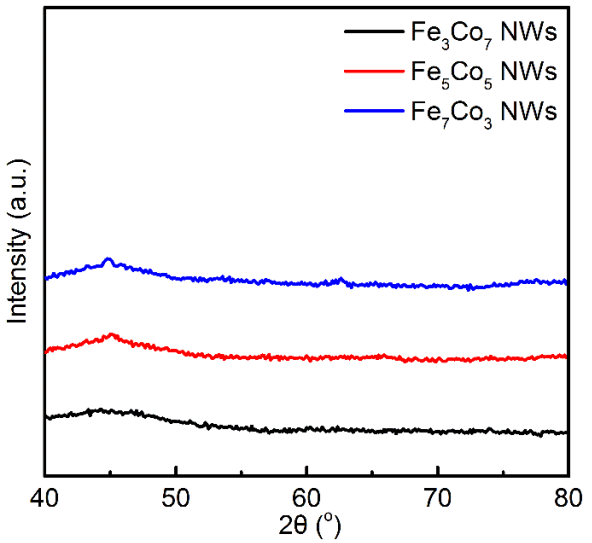

Fig. 2. XRD patterns of Fe_3Co_7 NWs, Fe_5Co_5 NWs and Fe_7Co_3 NWs.

three samples. The reason can be attributed to uncompleted crystallization with less hydrothermal reaction time. HRTEM image and SAED pattern were further elucidated on FeCo NWs innermicrostructures of FeCo NWs, being selected Fe_5Co_5 NWs as a case. The TEM image confirms hierarchy micro/nanostructures of Fe_5Co_5 NWs, being consistent with the same average diameter from SEM image results. Figure 3(a) presents wire-like Fe_5Co_5 NWs with substructured Fe_5Co_5 NPs. However, the innerinterfaces of adjacent Fe_5Co_5 NPs were blurry, emerging no-crystalline boundary. Inset SAED pattern exhibits a halo ring without any identified diffraction spots from Fe and Co. Further noncrystalline confirmation comes from the HRTEM image [Fig. 3(b)] with no measurable lattice fringes in the Fe_5Co_5 NWs, being confirmed with the same investigation on XRD results. Figures 3(c)–3(e) show the elemental mapping of Fe and Co in the Fe_5Co_5 NWs. Both the colors represented as Fe and Co were well dispersed in the selected area. Besides, it shows the quite same overlapped shapes of Fe/Co atoms distributions, revealing designed mole ratio achievement (Fe:Co = 1:1) in the observed Fe_5Co_5 NWs.

3.2. *Magnetic properties*

Magnetic loss, as one of the principal EMW losses, is acutely influenced by the inherent magnetic properties of ferromagnetic metals absorbers. Figure 4 shows the magnetic hysteresis curves of three FeCo NWs samples. Typical S-formed magnetic hysteresis curves can be found in all three FeCo NWs samples, presenting ferromagnetic behaviors. Because the changes of Fe/Co elemental ratios, the saturation magnetization (M_s) is 72.63 emu g^{-1} for Fe_3Co_7 NWs, 92.20 emu g^{-1} for Fe_5Co_5 NWs and 118.96 emu g^{-1} for Fe_7Co_3 NWs, separately. Because fine surface antiferromagnetic oxidation and spin disorder are induced by the nanosized effect and amorphous structure of Fe_5Co_5 NWs. M_s value

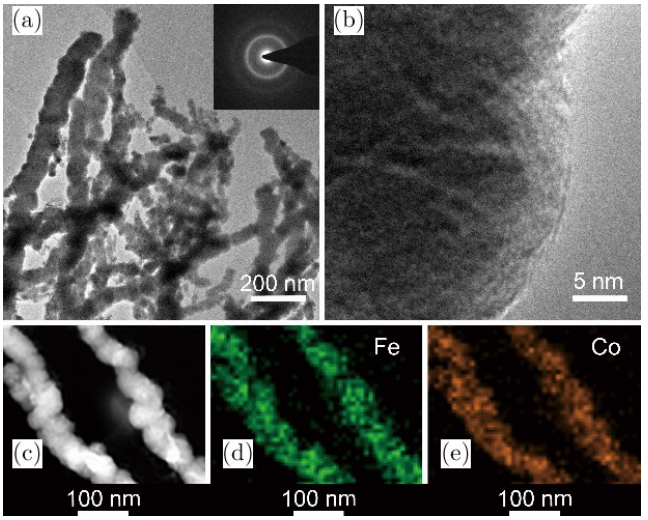

Fig. 3. TEM and elemental analysis of Fe_5Co_5 NWs. (a) Low-magnification HRTEM image. (The inset is SAED pattern.); (b) high-magnification HRTEM image and (c–e) EDS mappings.

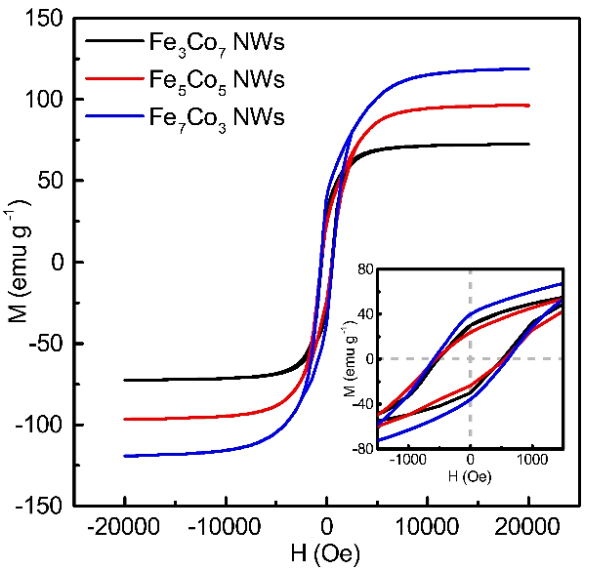

Fig. 4. Magnetic hysteresis curves of three FeCo NWs. (The inset image presents the high-magnification M–H curves.).

of Fe_5Co_5 NWs is lower than those of bulk Fe_5Co_5 alloy[17] and other highly crystallized Fe_5Co_5 nanostructures.[20,42] Another factor, being denoted as ferromagnetic resonance frequency, can be expressed with the following equations[43]:

$$K = \mu_0 M_s H_c/2, \tag{5}$$

$$H_a = 4|K|/3\mu_0 M_s, \tag{6}$$

$$2\pi f_r = rH_a, \tag{7}$$

where μ_0 represents free space permeability ($4\pi \times 10^{-7}\,\mathrm{H\,m^{-1}}$), K is the constant of anisotropic magneto-crystalline and r is the gyromagnetic ratio of the absorbent. Higher H_c is benignant to enlarge EMW absorption range in the high region of frequency. The inset presents the larger H_c is obtained in Fe_3Co_7 NWs with the value of 592.92 Oe, compared to the other two FeCo NWs. Specifically, the H_c values are negatively related to the increasing Fe content. This is because of restraining the inherent large H_c of Co metal with the increase of Fe element content. Further details of magnetic properties are shown in Table 1.

3.3. *Microwave absorption performance*

Figure 5(a) shows the RL intensity of FeCo NWs under 3-mm coating thickness as the designated thickness. The RL peaks of Fe_3Co_7 NWs, Fe_5Co_5 NWs, and Fe_7Co_3 NWs are −25.88 dB at 4 GHz, −19.06 dB at 4.24 GHz, and −21.98 dB at 5.44 GHz, respectively. In practical EM absorption utilization, the corresponding efficient absorption bandwidth ($f_E < -10$ dB) is equally important to the RL intensity, meaning fault tolerance of the absorbents for the microwave absorption aim. The value of f_E is located in both the low (2–7 GHz) and high frequency (12–18 GHz) with slight drifts in three samples. The f_E of Fe_3Co_7 NWs is occupied as 5.40 GHz for Fe_3Co_7 NWs (3.60–4.32 GHz; 13.32–18 GHz), while the one of Fe_5Co_5 NWs and Fe_7Co_3 NWs is 3.52 GHz (3.56–4.78 GHz; 15.18–17.48 GHz) and 4.91 GHz (4.58–6.47 GHz; 12.63–14.51 GHz; 16.86–18 GHz), respectively. Further contour map [Figures 5(b)–5(d)] shows three FeCo NWs RL absorption behaviors with continuous coating thickness changes from 1 mm to 5 mm. Fe_3Co_7 NWs show a larger f_E of 4.68 GHz in the high GHz range from 13.32 GHz to 18 GHz. Its f_E relatively shrinks in the 2–7 GHz range, compared to those of Fe_5Co_5 NWs and Fe_7Co_3 NWs (Fe_5Co_5 NWs: 2–5.50 GHz; Fe_7Co_3 NWs: 2.83–6.94 GHz). Overall, microwave absorption intensity and f_E values strongly rely on the Fe/Co atomic ratios, making tunable EMW absorption properties attainable. Fe_3Co_7 NWs hold a narrow f_E in the low frequency and a broad f_E in the high frequency, while the circumstance of f_E is opposite in the Fe_7Co_3 NWs. A moderate f_E is obtained in Fe_5Co_5 NWs, which is complementary between Fe_7Co_3 NWs and Fe_3Co_7 NWs. A brief comparison between our FeCo NWs and other FeCo-based absorbers is also present in Table 2. Although the minimum RL values of FeCo NWs are lower than other unique FeCo-based absorbers, microwave absorption performances of FeCo NWs are comparable with the flexible range of f_E. Our amorphous FeCo NWs' absorbers are enhanced with the flourishing of defect polarizations to tune the areas of f_E while the crystalized FeCo-based ones present the higher intensity of the RL values due to their high electrical conductivity for conductive loss. Besides, the absence of promoted dielectric loss from secondary carbon-based medium and different nanostructures are another parameters to be responsible for the RL changes of FeCo NWs in our work, being distinctive to as-mentioned reports.[8,20,44–47]

Figures 6(a)–6(d) show complex permittivity and permeability with the changes of real and imaginary part. First, checking permittivity [Fig. 6(a)], three FeCo NWs show quite the same fluctuations with the differences of ε' intensities. ε' rapidly increases to the peak value of 39.37 and sharply decreases to 1.70 around in the rest frequency range for Fe_3Co_7 NWs, while the ε' peak of Fe_5Co_5 NWs is 21.08 and that of Fe_7Co_3 NWs is 11.85. The similar changes are also observed in the imaginary part of permittivity for these samples. The ε'' values [Fig. 6(b)] gradually increase to the maximum peaks with the value of 38.20 for Fe_3Co_7 NWs at 7.37 GHz, 21.80 for Fe_5Co_5 NWs at 8.15 GHz and 12.03 for Fe_7Co_3 NWs at 9.08 GHz, respectively. Then, ε'' values of three samples return to the lower values of 1.57–5.05. Operation of the free electron theory

Table 1. Magnetic properties of FeCo NWs.

Samples	M_s (emu g^{-1})	M_r (Oe)
Fe_3Co_7 NWs	72.63	521.61
Fe_5Co_5 NWs	92.20	554.96
Fe_7Co_3 NWs	118.96	592.92

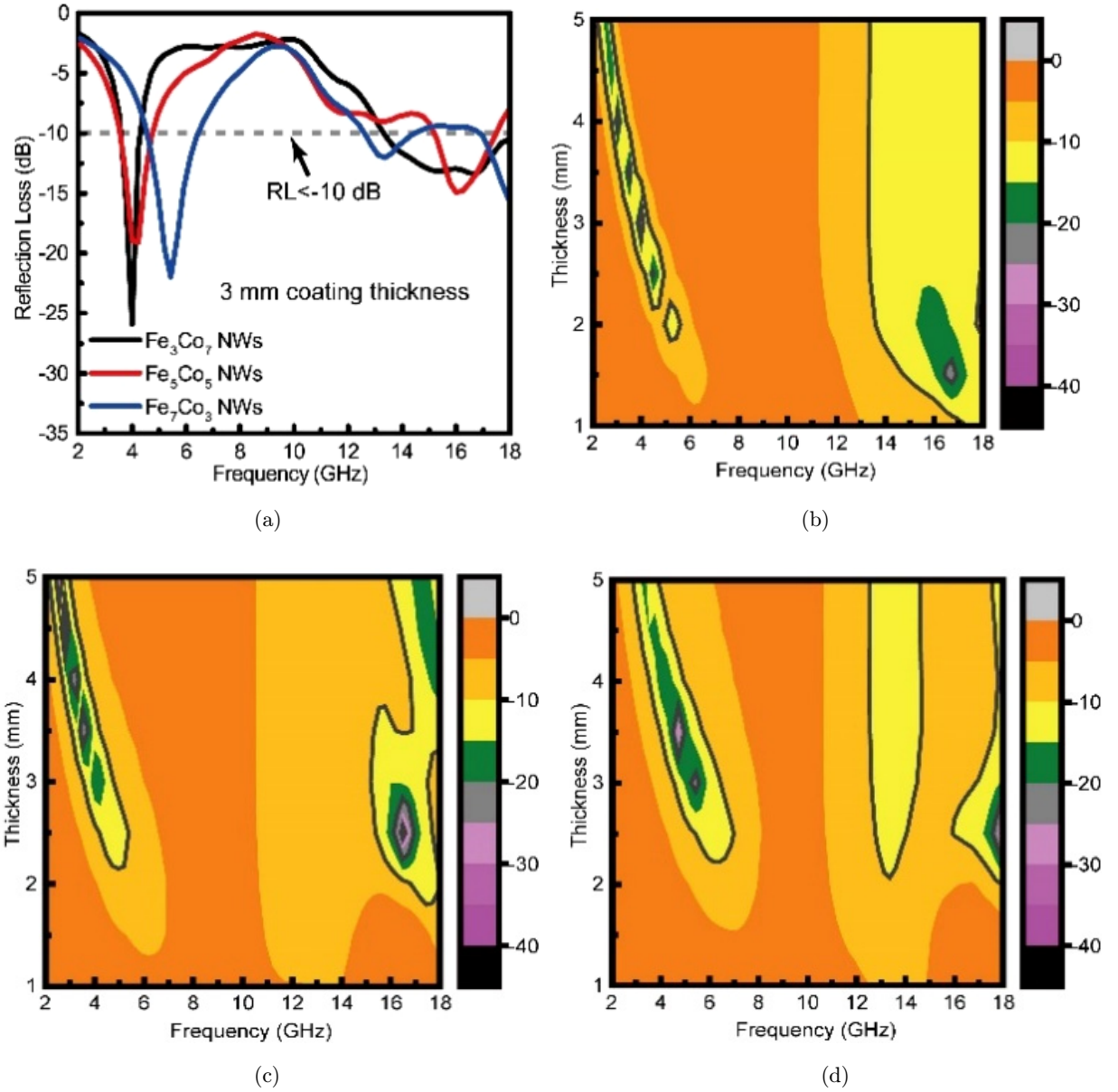

Fig. 5. (a) RL curves of three FeCo NWs absorbers under 3 mm coating thickness; RL contour maps of Fe_3Co_7 NWs (b), Fe_5Co_5 NWs (c) and Fe_7Co_3 NWs (d).

Table 2. A comparison of microwave absorption performance in recent FeCo-based absorbers.

Samples	Fe/Co ratio	Minimum RL (dB)	Corresponding peak (GHz)	Range of f_E (GHz)	Thickness (mm)	Reference
Dendritic-like $Fe_{0.7}Co_{0.3}$	7:3	−36.7	9.2	About 8.0–11.0	1.4	20
FeCo nanocube	5:5	−26.2	3.8	2.8–5.1; 11.2–13.2	3.5	44
Hexagonal-cone like $Fe_{50}Co_{50}$ alloy	5:5	−22	10.4	10.5–17.6	1.5	45
Cone-like Fe_7Co_3 alloys	7:3	−53.6	14.3	11.2–18	1.55	46
FeCo-C core-shell NPs	1:1	−56.0	11.7	11.7–17.9	2	47
FeCo/C composites	4:6	−43.8	13.7	11.36–17.36	2	48
Fe_3Co_7 NWs	3:7	−25.88	4.0	3.60–4.32; 13.32–18	3	This work
Fe_5Co_5 NWs	5:5	−19.06	4.24	3.56–4.78; 15.18–17.48	3	This work
Fe_7Co_3 NWs	7:3	−21.98	5.44	4.58–6.47; 12.63–14.51; 16.86–18	3	This work

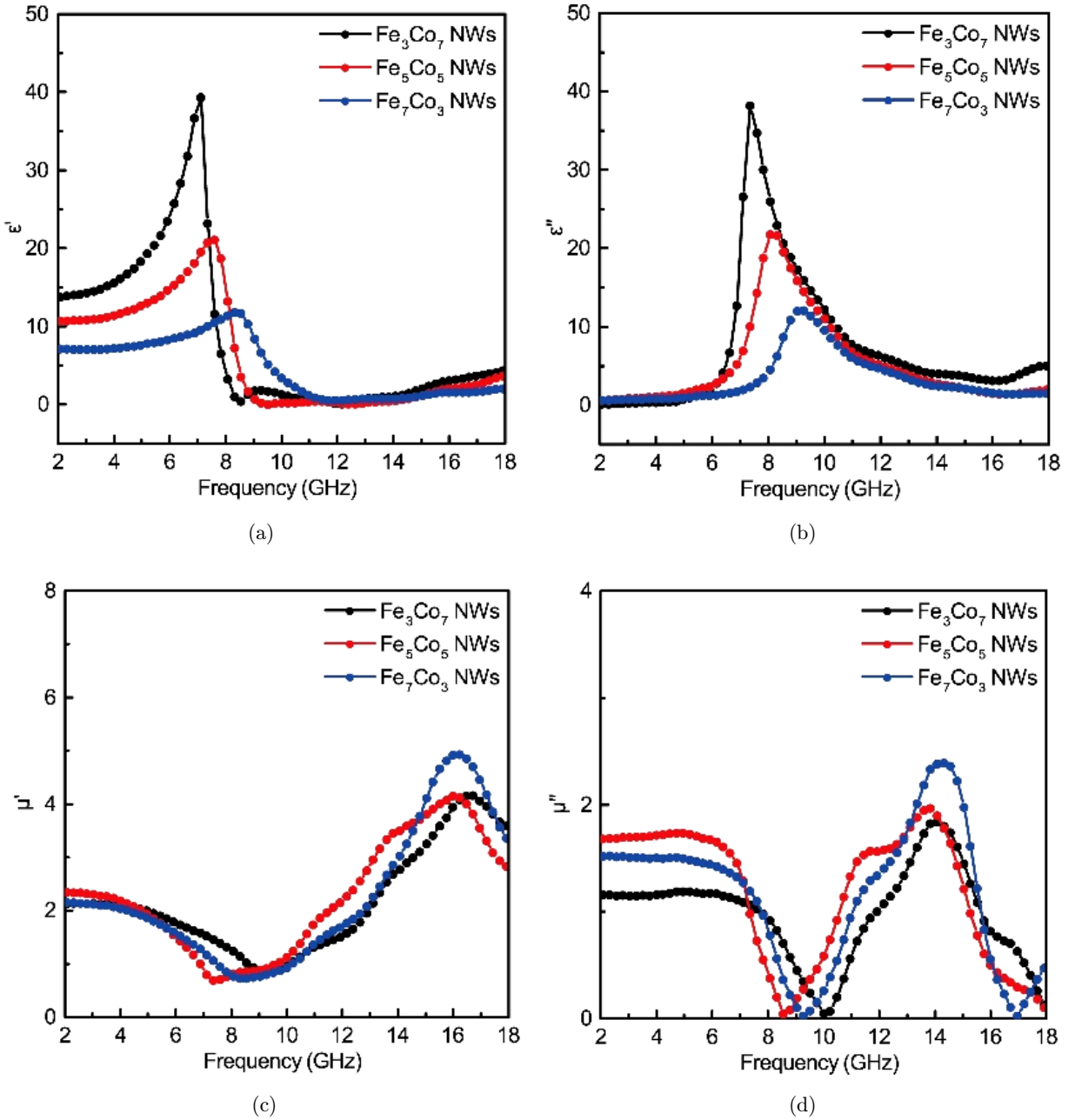

Fig. 6. Frequency dependence of complex permittivity and permeability of FeCo NWs absorbers. Real parts (a) and imaginary parts (b) of the permittivity; real parts (c) and imaginary parts (d) of the permeability.

($\varepsilon'' = 1/2\pi\varepsilon_0\rho f$)[44] can explain the same tendencies of ε' and ε'' peaks in these three FeCo NWs. Thanks to a better electrical conductivity of Co (Co: 1.80×10^7 S m^{-1}, Fe: 1.17×10^7 S m^{-1}),[48] higher ε' and ε'' can be gained in Co-rich FeCo NWs. It is an alternative way to realized for tuning conductive loss in FeCo NWs, comparing to use second highly-conductive mediums directly.[46,47] It depends on wire-like micro/nanostructures and inherent metallic property for forming an interconnected conductive network. Due to the ferromagnetic behaviors of FeCo NWs as previous magnetic investigation, the magnetic loss is the other important parameter for effecting EMW absorption performances of FeCo NWs. Figures 6(c) and 6(d) show the complex permeability variations in the Fe_3Co_7 NWs, Fe_5Co_5 NWs, and Fe_5Co_5 NWs absorbents. Both μ' and μ'' of three samples present relatively high values in both the low (2–7 GHz) and high range of frequency (12–18 GHz), compared to the

rest frequency. Although the imaginary parts of permittivity and permeability have been explanation some extent of the dielectric/magnetic loss, loss tangents often replace them, as the more accurate factors, to evaluate both dielectric and magnetic loss. Because the dielectric loss tangent ($\tan\delta_\varepsilon = \varepsilon''/\varepsilon'$) and magnetic loss tangent ($\tan\delta_\mu = \mu''/\mu'$) are fully considered the relationships between the real and imaginary parts of permittivity and permeability in the absorbers.[15,20,30] Figure 7 presents the dielectric/magnetic loss tangents of three FeCo NWs absorbers. Both dielectric/magnetic loss tangents of all the samples present strong dielectric/magnetic loss in the low-frequency range (around 3.5–8 GHz) and high-frequency range (around 13–18 GHz). The resonant peaks can be easily found in these areas, presenting strong defect relaxations and interfacial polarizations. The different intensities of loss tangents might be suffered from the effects of Fe/Co ratio. For observing the low-frequency range, the maximum dielectric loss tangent is 1.43 in Fe_3Co_7 NWs, compared with other two FeCo NWs. While Fe_7Co_3 NWs obtain the peak of dielectric loss tangent, which is 1.88. The maximum dielectric loss tangents are 1.43 for Fe_3Co_7 NWs and 1.88 for Fe_7Co_3 NWs in the low/high-frequency ranges, respectively. While it presents the maximum magnetic loss tangent is 1.62 for Fe_5Co_5 in the low-frequency range, comparing with the other two FeCo NWs. Three FeCo NWs show quite equal values of magnetic loss tangents in the high-frequency range. The improved resonant areas, which are in both dielectric and magnetic loss tangents, partially contribute to the bandwidth of f_E and related intensity of RL, being consistent with the results of Fig. 5. Meantime, the values of dielectric/magnetic loss tangents are low in the middle frequency (8–12 GHz), implying the inferior loss abilities for microwave absorption performances of FeCo NWs.

In general, ferromagnetic alloy absorbers contain the multimagnetic losses such as domain wall resonance, exchange and natural resonance, dimensional resonances, and eddy current loss.[8,10,46] Among them, the eddy current produces the subordinate innermagnetic field to counteract the external magnetic field, which greatly impairs absorption. It especially harms the high range of frequency in the ferromagnetic absorbers.[49] The related skin effect makes the induced current on the absorber surface, wasting the EMW absorption potency in the internal absorbers. Thus, it is crucial to understanding the fact that whether or not the magnetic loss mechanism is affected by eddy current. Here eddy current effect is marked as C_0 ($C_0 = \mu''(\mu')^{-2}f^{-1}$) for studying as presented in Fig. 8. In general, when eddy-current effect is responsible for the magnetic loss, C_0 is constant like a straight line in the curve of C_0 versus f. It clearly exhibits continuous variations in all three FeCo NWs absorbers, implying little influences from eddy current. It might be attributed to the contribution of amorphous structure

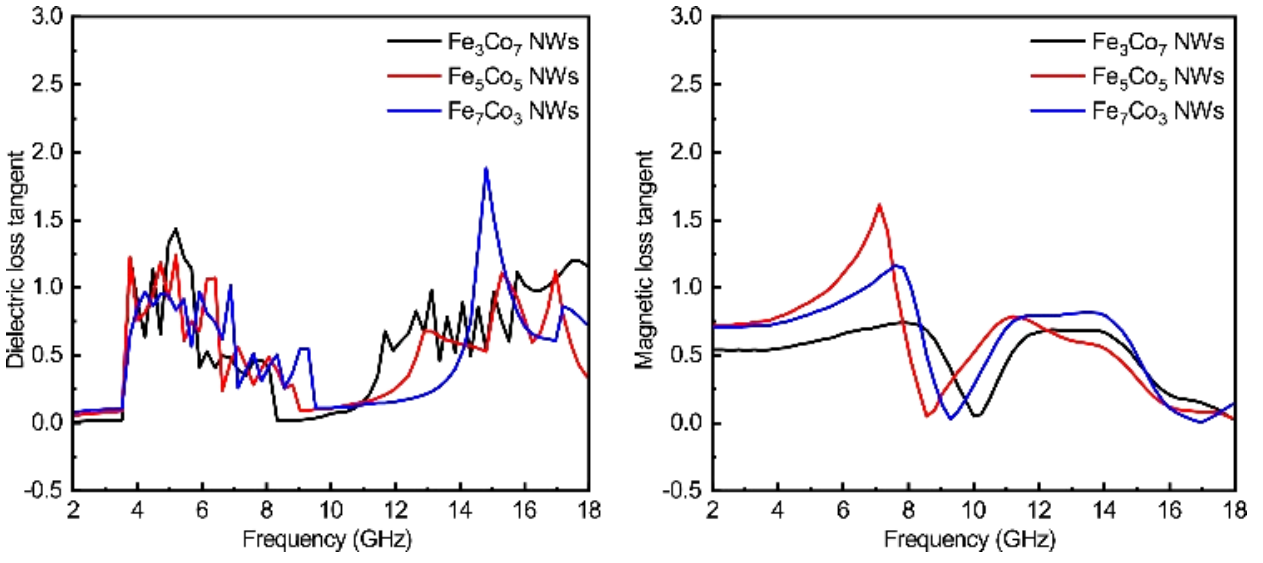

(a) (b)

Fig. 7. Dielectric loss tangents (a) and magnetic loss tangents (b) of three FeCo NWs absorbers.

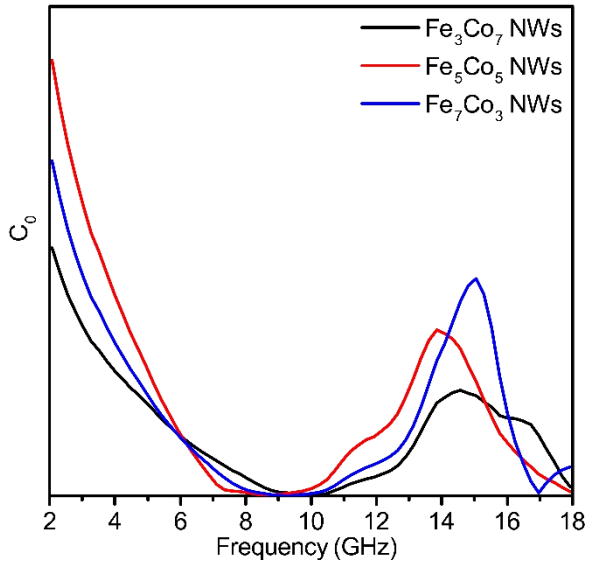

Fig. 8. Eddy current losses of three FeCo NWs absorbers.

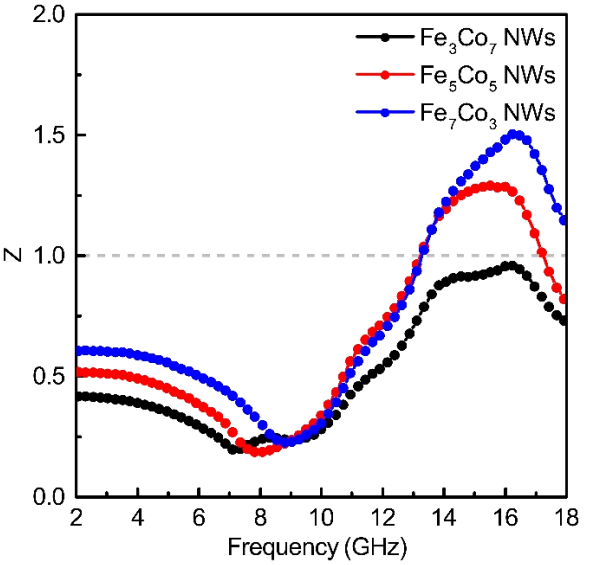

Fig. 9. Impedance matching values of Z.

that can prevent the disruption of eddy current,[50] maintaining the high-performance EMW absorption in the high frequency for the absorbers.

Impedance matching is another significant parameter to meet good EMW absorption performance, which can be interpreted with the following equations[51]:

$$Z = Z_1/Z_0, \tag{8}$$

$$Z_1 = (\mu_r/\varepsilon_r)^{1/2} Z_0, \tag{9}$$

where ε_r and μ_r are responsible for the complex permittivity and permeability of the absorbent. Z_1 and Z_0 execute as the impedance value of the material and free space, respectively. When Z is equal to 1, the absorber obtained the best impedance matching, making all incident wave into the interior of the absorber. Figure 9 exhibits the changes of Z values in the three samples. The Z values are positively correlated to the Fe atoms increase in the low frequency (2–6 GHz). Z values of Fe_7Co_3 NWs are much closer than the other two FeCo NWs for the ideal value ($Z = 1$). While the situation of the Z value becomes sophisticated in the high-frequency range (14–18 GHz). The Z value of Fe_5Co_5 NWs is almost reached to 1 in the 17.26 GHz. While Z values of Fe_3Co_7 NWs are much better than one of Fe_7Co_3 NWs. Scoping all frequency (2–18 GHz), Fe_5Co_5 NWs obtain the moderate Z values, being close to the perfect impedance matching ($Z = 1$). In general, the minimum RL values, the frequency of corresponding RL peak and the range of bandwidths ($f_E < -10$ dB) are equally important to evaluate the RL parameter for the microwave absorption performances. Although all the FeCo NWs obtain the minimum RL in the low-frequency bandwidth (−25.88 dB for Fe_3Co_7 NWs; −19.06 dB for Fe_5Co_5 NWs; −21.98 dB for Fe_7Co_3 NWs) under 3 mm thickness. However, the inferior f_E bandwidths of three samples are found in the lower frequency, which involves the lessen contributions of Z values in this frequency range (Table 2). The other factor is the nexus between loss abilities and impedance matching, which greatly affects the intensity of RL peak and corresponding f_E bandwidths. As a case, Fe_3Co_7 NWs show the mismatching between RL peak and range of f_E bandwidth under 3 mm thickness. Nonetheless, rational controlling the Fe/Co atomic ratios is achieved for the different EM absorption demands with the full consideration of containing the changes of loss tangents and Z values.

It can be concluded as-prepared amorphous FeCo NWs meet versatile EM wave absorption demands with precisely controlling atomic ratios of Fe and Co. Figure 10 illustrates proposed microwave absorption mechanism in the FeCo NWs absorbers. Based on the isotropic antenna mechanism,[22,24] flourished microcurrent networks are in favor of conductive loss, due to the advantages of wire-like micro/nanostructures in three samples. For improving the transferring and attenuating time, the amorphous structures supply sufficient defects to trap the incident waves for prolonging detention

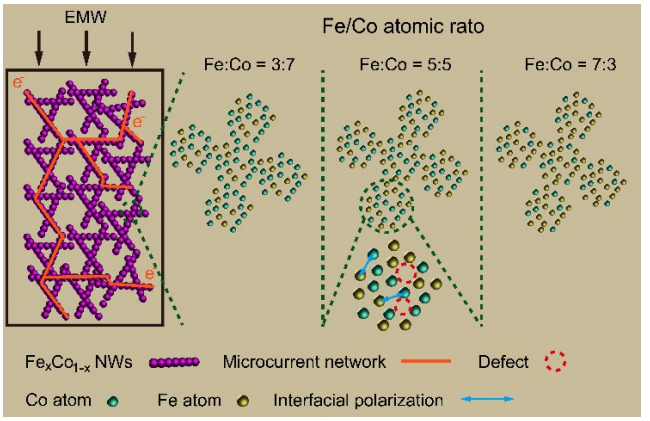

Fig. 10. Schematic presentation of enhanced EMW absorption mechanism in the FeCo NWs absorbers.

time in the absorbers interiors. Merits of vacancies, being originated from interconnected wire-like networks and defects, can also improve impedance matching behavior. Moreover, tuning the Fe/Co atomic ratios not only acts on the changes of the magnetic properties for the magnetic loss but also fairly changes the displacement between Co and Fe atoms. As a case for Fe_5Co_5 NWs, ample interfaces between Co and Fe atoms improve the interfacial polarization for dielectric loss. The balance between the saturation magnetization and coactivity is achieved for boosting magnetic loss. All these excellences give a decent EMW absorption performance of FeCo NWs absorbents, being comparable to using second mediums in FeCo-based absorbers.[46,47,52,53] Two factors, including amorphous wire-like micro/nanostructures and magnetic properties regulating of Fe/Co elemental ratio, can be ascribed to tuning electric/magnetic losses and efficacy of impendence matching in the FeCo NWs.

4. Conclusions

In summary, a template-free synthesis of amorphous FeCo NWs was prepared via MFA hydrothermal approach. Such FeCo NWs own the radial diameter of $\sim$120 nm and the average length of 3–5 μm, respectively. Such FeCo NWs have been satisfied different frequency range of absorption demands through changing atomic ratios of Fe/Co. For example, under 3 mm coating thickness, the efficient EMW absorption bandwidth is covered with a range of 5.40 GHz in Fe_3Co_7 NWs, while the one of Fe_5Co_5 NWs and Fe_7Co_3 NWs is 3.52 GHz and 4.91 GHz, respectively. It is contributed from cooperative enhancements of electromagnetic losses properties and impedance matching for decent microwave absorption properties in the amorphous FeCo NWs absorbers. This work also provides an alternative pathway for fabricating amorphous bimetallic NWs absorbers.

Acknowledgments

This work is financially supported by the National Natural Science Foundation of China (Grant Nos. 11632005 and 11772109) and the Foundation for Innovative Research Groups of the National Natural Science Foundation of China (Grant No. 11421091).

References

1. Q. Yin, H. Xing, R. Shu, X. Ji, D. Tan and Y. Gan, *Nano* **11**, 1650058 (2016).
2. B. B. Zhang, P. F. Wang, J. C. Xu, Y. B. Han, H. X. Jin, D. F. Jin, X. L. Peng, B. Hong, J. Li, J. Gong, H. L. Ge, Z. W. Zhu and X. Q. Wang, *Nano* **10**, 1550070 (2015).
3. R. W. Shu, M. Wang, Y. Y. Yang, S. Y. Chang, G. Y. Zhang, Y. Gan, J. J. Shi and J. He, *Nano* **12**, 1750144 (2017).
4. N. Li, G. W. Huang, Y. Q. Li, H. M. Xiao, Q. P. Feng, N. Hu and S. Y. Fu, *ACS Appl. Mater. Interfaces* **9**, 2973 (2017).
5. D. Estevez, F. X. Qin, L. Quan, Y. Luo, X. F. Zheng, H. Wang and H. X. Peng, *Carbon* **132**, 486 (2018).
6. X. Q. Guo, Z. Y. Bai, B. Zhao, R. Zhang and J. B. Chen, *J. Mater. Sci. Mater. El.* **27**, 8408 (2016).
7. N. Chen, J. T. Jiang, C. Y. Xu, Y. Yuan, Y. X. Gong and L. Zhen, *ACS Appl. Mater. Interfaces* **9**, 21933 (2017).
8. H. L. Lv, G. B. Ji, M. Wang, C. M. Shang, H. Q. Zhang and Y. W. Du, *J. Alloy. Compd.* **615**, 1037 (2014).
9. X. H. Li, J. Feng, Y. P. Du, J. T. Bai, H. M. Fan, H. L. Zhang, Y. Peng and F. S. Li, *J. Mater. Chem. A* **3**, 5535 (2015).
10. J. Zhou, Z. H. Zhu and C. Xiong, *J. Electron. Mater.* **47**, 1244 (2018).
11. Q. H Liu, X. H. Xu, W. X. Xia, R. C. Che, C. Chen, Q. Cao and J. G. He, *Nanoscale* **7**, 1736 (2015).
12. H. Zhao, Z. Zhu, C. Xiong, X. Xu and Q. Lin *J. Magn. Magn. Mater.* **422**, 402 (2017).
13. N. Chen, J. T. Jiang, C. Y. Xu, S. J. Yan and L. Zhen, *Sci. Rep.* **8**, 3196 (2018).
14. Q. H. Liu, Q. Cao, X. B. Zhao, H. Bi, C. Wang, D. S. Wu and R. C. Che, *ACS Appl. Mater. Interfaces* **7**, 4233 (2015)

15. H. Li, Z. Cao, J. Lin, H. Zhao, Q. Jiang, Z. Jiang, H. Liao, Q. Kuang and Z. Xie, *Nanoscale* **10**, 1930 (2018).
16. V. Sara Liébana, S. Ruslan, B. Cristina, M. P. Ester, V. Manuel, A. Behnaz, Y. Xiang, T. Peter, F. Josef, S. Marina, W. Ulf and F. Michael, *Nanotechnology* **26**, 415704 (2015).
17. D. W. Liu, R. Qiang, Y. C. Du, Y. Wang, C. Tian and X. J. Han, *J. Colloid. Inter. Sci.* **514**, 10 (2018).
18. X. G. Liu, D. Y. Geng, H. Meng, B. Li, Q Zhang, D. J. Kang and Z. D. Zhang, *J. Phys. D Appl. Phys.* **45**, 239501 (2012).
19. J. Yan, Y. Huang, P. B. Liu and C. Wei, *J. Mater. Sci. Mater. El.* **28**, 3159 (2017).
20. Z. X. Yu, N. Zhang, Z. P. Yao, X. J. Han and Z. H. Jiang, *J. Mater. Chem. A* **1**, 12462 (2013).
21. P. Wang, L. Cheng and L. Zhang, *Chem. Eng. J.* **338**, 248 (2018).
22. R. F. Zhuo, L. Qiao, H. T. Feng, J. T. Chen, D. Yan, Z. G. Wu and P. X. Yan, *J. Appl. Phys.* **104**, 094101 (2008).
23. H. X. Pan, X. W. Yin, J. M. Xue, L. F. Cheng and L. T. Zhang, *Carbon* **107**, 36 (2016).
24. H. F. Li, Y. H. Huang, G. B. Sun, X. Q. Yan, Y. Yang, J. Wang, Y. Zhang, *J. Phys. Chem. C* **114**, 10088 (2010).
25. G. Kinjal, T. Poching, C. Girija, P. Narayan, E. Kevin, C. Jun and J. P. Liu, *Nanotechnology* **26**, 075601 (2015).
26. S. Vock, C. Hengst, M. Wolf, K. Tschulik, M. Uhlemann, Z. Sasvari, D. Makarov, O. G. Schmidt, L. Schultz and V. Neu, *Appl. Phys. Lett.* **105**, 172409 (2014).
27. Y. M. Song, W. Lu, Y. W. Xu, J. D. Shi and X. M. Fang, *J. Alloy. Compd.* **652**, 179 (2015).
28. P. P. Jing, J. L. Du, J. B. Wang, Z. T. Zhu, H. M. Feng, Z. L. Liu and Q. F. Liu, *Mater. Lett.* **162**, 176 (2016).
29. J. Alonso, H. Khurshid, V. Sankar, Z. Nemati, M. H. Phan, E. Garayo, J. A. Garcia and H. Srikanth, *J. Appl. Phys.* **117**, 17D113 (2015).
30. H. L. Xu, X. W. Yin, M. Zhu, M. H. Li, H. Zhang, H. J. Wei, L. T. Zhang and L. F. Cheng, *Carbon* **142**, 346 (2019).
31. F. Peng, F. Meng, Y. Guo, H. Wang, F. Huang and Z. Zhou, *ACS Sustain. Chem. Eng.* **6**, 16744 (2018).
32. B. Quan, X. H. Liang, G. B. Ji, Y. Cheng, W. Liu, J. N. Ma, Y. N. Zhang, D. R. Li and G. Y. Xu, *J. Alloy. Compd.* **728**, 1065 (2017).
33. L. Wang, G. F. Gong, J. Y. Shen and J. S. Leng, *High Perform. Polym.* (2018), https://doi.org/10.1177/0954008318815733.
34. X. Jian, X. N. Chen, Z. W. Zhou, G. Li, M. Jiang, X. L. Xu, J. Lu, Q. M. Li, Y. Wang, J. H. Gou and D. Hui, *Phys. Chem. Chem. Phys.* **17**, 3024 (2015).
35. Z. B. Su, J. Tao, J. Y. Xiang, Y. Zhang, C. Su and F. S. Wen, *Mater. Res. Bull.* **84**, 445 (2016).
36. X. Wang, R. Gong, X. Li, Y. He, L. Liu, P. Li, *J. Mater. Sci. Mater. Election.* **18**, 481 (2006).
37. D. M. F. Santos and C. A. C. Sequeira, *Renew. Sustain Energy Rev.* **15**, 3980 (2011).
38. M. Hesani, A. Yazdani, B. Abedi Ravan and M. Ghazanfari, *Solid State Commun.* **150**, 594 (2010).
39. J. Kim, J. Kim, J. Kim and K. H. Kim, *J. Appl. Phys.* **113**, 17A313 (2013).
40. J. Y. Shen, Y. T. Yao, Y. J. Liu and J. S. Leng, *J. Mater. Chem. C* **4**, 7614 (2016).
41. S. Auer and D. Frenkel, *Nature* **413**, 711 (2001).
42. S. J. Yan, L. Zhen, C. Y. Xu, J. T. Jiang, W. Z. Shao and J. K. Tang, *J. Magn. Magn. Mater.* **323**, 515 (2011).
43. S. Ohkoshi, S. Kuroki, S. Sakurai, K. Matsumoto, K. Sato and S. Sasaki, *Angew. Chem. Int. Ed.* **46**, 8392 (2007).
44. Yan, Y. Huang, P. B. Liu and C. Wei, *J. Mater. Sci. Mater. Electron.* **28**, 3159 (2017).
45. Y. Cheng, G. B. Ji, Z. Y. Li, H. L. Lv, W. Liu, Y. Zhao, J. M. Cao and Y. W. Du, *J. Alloy. Compd.* **704**, 289 (2017).
46. D. R. Li, B. S. Zhang, W. Liu, X. H. Liang and G. B. Ji, *Dalton Trans.* **46**, 14926 (2017).
47. B. B. Liang, S. L. Wang, D. T. Kuang, L. Z. Hou, B. W. Yu, L. W. Lin, L. W. Deng, H. Huang and J. He. *Nanotechnology* **29**, 085604 (2018).
48. W. M. Haynes. CRC Handbook of Chemistry and Physics, 97th edn. (CRC Press, Boca Raton, 2017), pp. 2117–2118.
49. C. L. Zhu, M. L. Zhang, Y. J. Qiao, G. Xiao, F. Zhang and Y. J. Chen, *J. Phys. Chem. C* **114**, 16229 (2010).
50. R. C. Che, L. M. Peng, X. F. Duan, Q. Chen and X. L. Liang, *Adv. Mater.* **16**, 401 (2004).
51. H. L. Lv, H. Q. Zhang, G. B. Ji and Z. J. Xu, *ACS Appl. Mater. Interfaces* **8**, 6529 (2016).
52. D. R. Li, X. H. Liang, W. Liu, J. N. Ma, Y. N. Zhang, G. B. Ji and W. Meng, *J. Colloid. Inter. Sci.* **507**, 131 (2017).
53. X. M. Zhang, G. B. Ji, W. Liu, B. Quan, X. H. Liang, C. M. Shang, Y. Cheng and Y. W. Du, *Nanoscale* **7**, 12932 (2015).